A quantitative assessment of the damage mechanisms of CFRP laminates interleaved by PA66 electrospun nanofibers using acoustic emission

Mohammadi, Reza; Ahmadi Najafabadi, Mehdi; Saghafi, Hamed; Saeedifar, Milad; Zarouchas, Dimitrios

DOI
10.1016/j.compstruct.2020.113395

Publication date
2021

Document Version
Final published version

Published in
Composite Structures

Composite Structures 258 (2021) 113395

Contents lists available at ScienceDirect

Composite Structures

journal homepage: www.elsevier.com/locate/compstruct

A quantitative assessment of the damage mechanisms of CFRP laminates interleaved by PA66 electrospun nanofibers using acoustic emission

Reza Mohammadi [a], Mehdi Ahmadi Najafabadi [a,*], Hamed Saghafi [b,c], Milad Saeedifar [d], Dimitrios Zarouchas [d]

[a] Non-destructive Testing Lab, Department of Mechanical Engineering, Amirkabir University of Technology, Tehran, Iran
[b] Department of Mechanical Engineering, Tafresh University, Tafresh, Iran
[c] New Technologies Research Center (NTRC), Amirkabir University of Technology, Tehran, Iran
[d] Structural Integrity & Composites Group, Faculty of Aerospace Engineering, Delft University of Technology, Delft, the Netherlands

ARTICLE INFO

Keywords:
Composite laminates
Damage mechanisms
Nanofiber
Acoustic emission
Fracture modes

ABSTRACT

Interleaving composite laminates with nanofibrous mat is one of the most reliable methods for increasing interlaminar fracture toughness. The present study seeks to find out how the damage mechanisms of carbon fiber reinforced polymers (CFRPs), subjected to the mode-I and mode-II fracture tests, are affected while those are modified by interleaved Polyamide 66 (PA66) electrospun layers. For this goal, acoustic emission (AE) and scanning electron microscope (SEM) techniques were used for assessing the damage mechanisms. The mode-I test results showed that adding nanofibers could decrease matrix cracking, fiber breakage, and fiber/-matrix debonding by 92%, 27%, and 87%, respectively. The AE demonstrated that no fiber breakage occurred during mode-II loading in both non-modified and nanomodified specimens which was validated by SEM images. On the other hand, the two oth0er damage modes, i.e. matrix cracking and fiber/matrix debonding, decreased about 97% in the nanomodified laminates.

1. Introduction

Despite the key advantages of carbon fiber reinforced polymers (CFRPs), such as high specific strength and stiffness, high corrosion resistance, and high fatigue life, they are suffered from poor interlaminar strength. This fact leads to inducing interlaminar cracks, delamination, in these materials under loading conditions, and they significantly affect the integrity of the composite structure. Besides delamination, other damage mechanisms such as matrix cracking, fiber/matrix debonding, and fiber breakage are usually observed in damaged composite laminates. Based on the loading conditions, layup, boundary conditions, environmental conditions, materials, and adhesion quality between fibers and matrix, one or a combination of these damage mechanisms may occur in laminated composite structures [1]. Thus, these materials usually exhibit a complicated damage behavior which raises the need for a powerful technique to investigate their damage state. To this aim, among structural health monitoring (SHM) techniques, acoustic emission (AE) technique has shown excellent potential for fully characterizing these damage mechanisms in laminated composites, i.e. damage initiation detection, damage identification, damage severity assessment, and damage localization [2–6].

Different toughening techniques have been proposed to increase the resistance of composite laminates against delamination, i.e. the interlaminar fracture toughness [7–10]. Among these techniques, applying nanofibrous mat between composite layers has been attractive for researchers [11–14], and as unlike the other methods, such as Z-pinning, they do not adversely affect in-plane mechanical properties of the laminate [15]. Various types of nanofibers have been applied for this aim, such as polysulfone (PSF) [16–18], polycaprolactone (PCL) [19–22], polyvinylidene fluoride (PVDF) [23–25], and polyvinyl butyral (PVB) [26–28]. It has been proved that each polymer proposes a specific toughening mechanism to increase the fracture toughness. For instance, when PSF or PCL nanofibers are added to the epoxy, the nanofibers are converted to spherical particles and are dispersed uniformly in the epoxy during the curing process. These particles restrict the crack propagation and consequently more energy is required for the crack growth [24].

According to the review paper published by Saghafi et al. [29], it was shown that Polyamide 66 (PA66) is one of the best choices for the toughening of CFRPs. Many studies have been conducted in this field, and the influence of nanofibers on fracture response of composite laminates has been investigated in different aspects [30–33]. Brugo

* Corresponding author.
E-mail address: ahmadin@aut.ac.ir (M. Ahmadi Najafabadi).

https://doi.org/10.1016/j.compstruct.2020.113395
Received 21 May 2020; Revised 8 October 2020; Accepted 30 November 2020
Available online 2 December 2020

and Palazzetti [34] considered the effect of nanomat thickness on modes I and II of unidirectional (UD) and woven carbon/epoxy laminates. The results showed that the increase of nanomat thickness led to the enhancement of the fracture toughness of the woven specimens, while the UD specimens were less affected by nanofibers. In another study, Palazzetti et al. [35] considered the effect of the geometrical features of the PA66 electrospun nanofibers, i.e. their orientation, nanolayer thickness, and nanofibers' diameter, on the mode-I and mode-II fracture toughness of carbon/epoxy specimens. They showed that a thick interleaf layer can decrease the fracture toughness because of the presence of a huge number of porosities left in the nanolayer after the curing process. In addition, the smaller diameters of the nanofibers led to the increase of the energy absorbing capability of the specimens. The nanofibers orientation showed different effects depending on the fracture mode. In another study, Palazzetti et al. [36] used AE for investigating the fracture behavior of carbon/epoxy laminates interleaved by PA66. They analyzed the overall AE activity of the specimens but without classifying and correlating the AE data to different damage mechanisms. The mechanical results showed that the PA66 mitigated the initiation and propagation of delamination and the AE showed that nanomodified specimens released less AE activities than the reference specimens.

Although, some studies have been performed on CFRPs interleaved by PA66, they were mainly concentrated on the fracture toughness assessment and there is still a gap for the quantitative evaluation of the effect of these nanofibers on the different damage mechanisms. Therefore, the present study tries to quantify the effect of PA66 on the different damage mechanisms of modified carbon/epoxy composites using the AE and scanning electron microscope (SEM) techniques which helps better understanding of the toughening mechanisms of these nanofibers.

2. Materials, manufacturing and testing

2.1. Electrospinning method

Fibers with diameters ranging from nanometer to micrometer scale can be produced using the electrospinning method. As shown in Fig. 1A, an electrospinning setup consists of:

The high voltage power supply,
The syringe (with a metallic needle) and the pump for injecting the solution,
The collector.

In this process, a high voltage is first applied to the polymeric solution; then, a pendant droplet is formed at the tip of the needle. Due to the presence of the electrostatic field between the needle tip and the collector, the pendant droplet is deformed into a conical shape (known as the Taylor cone). When the electrostatic force is enough to overcome the surface tension of the Taylor cone, a fine jet of solution comes out from the tip of the needle. On the way from the needle tip to the collector, the solvent evaporates and finally a long and thin solidified filament is deposited onto the collector, resulting in the formation of a uniform micro or nanofiber. For producing nanofiber, the PA66 polymer (Zytel E53NC010 (supplied from DuPont, was used. The molecular weight of this polymer is 226.32 gr/mol.

The electrospinning process parameters of the collector rotational speed, the applied voltage, and distance between the collector and the needle tip were selected 100 rpm, 28 kV, and 12 cm, respectively. The solution was prepared by adding 20% w/v PA66 pellets in the solvents of formic acid and 2.2.2-Trifluoroethanol with the ratio of 30/70 v/v. The SEM image of the produced nanofibers is depicted in Fig. 1B.

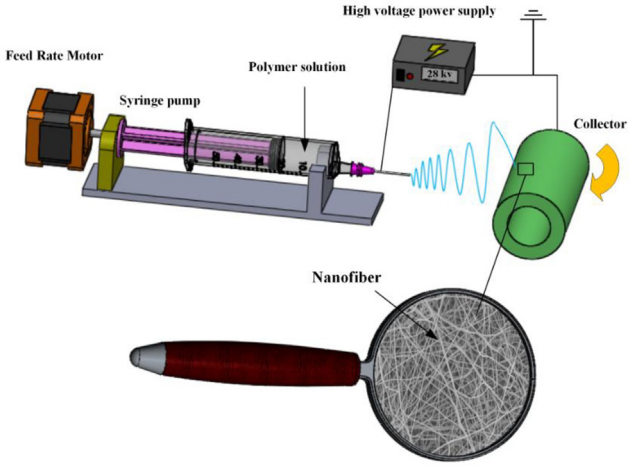

(A)

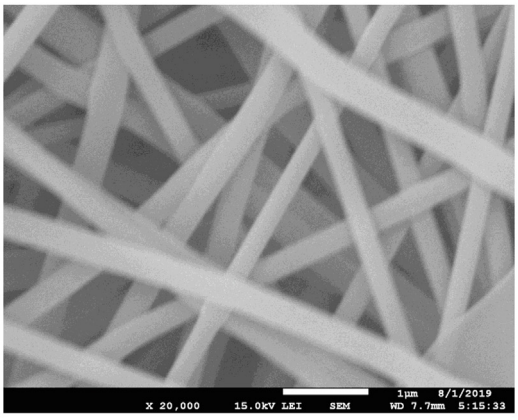

(B)

Fig. 1. A) A schematic of the electrospinning process, and B) the SEM image of the produced nanofiber mat.

2.2. Lamination

The test specimens were laminated of 24 layers of Hexcel AS4/8552 unidirectional prepreg sheets, from Hexcel ® Corporation. The specifications of this prepreg are presented in Table 1. A thin Teflon film with a thickness of 12.7 μm was placed between 12th and 13th layers to create the initial delamination; subsequently, the 50 μm-electrospun mat was implanted at the side of Teflon film at the same layer. The curing process was performed according to Fig. 2 in which the maximum temperature and pressure were 180 ℃ and 7 bar [37]. As it is clear from the microscopic image from the lateral side of the specimen (Fig. 3A & B), the real thickness of the nano-

Table 1
The specifications of the AS4/8552 prepreg.

Properties	Unit	Value
Fiber density	g/cm^3	1.79
Filament count/tow	–	12 K
Resin density	g/cm^3	1.30
Nominal cured ply thickness	mm	0.130
Nominal fiber volume	%	57.42
Nominal laminate density	g/cm^3	1.58

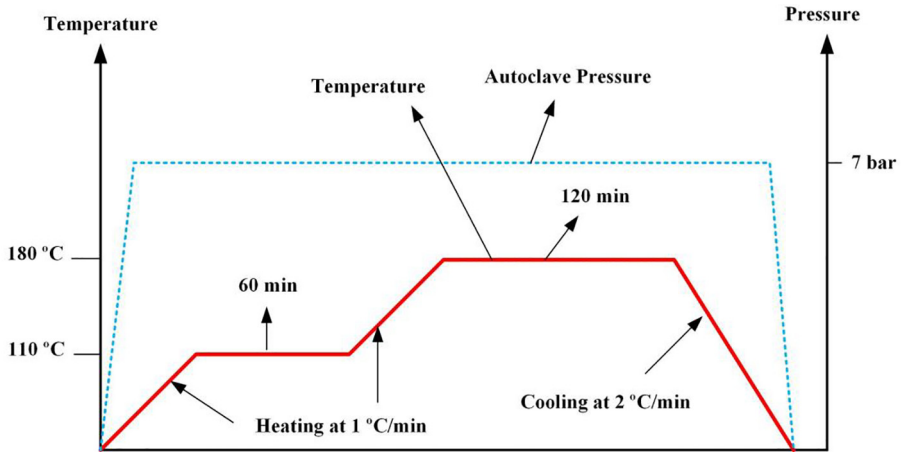

Fig 2. The curing process of the laminate.

mat is ~50 μm. In order to investigate the penetration and impregnation of resin into the nanofibers mat, the SEM method was used. As seen in Fig. 3C, impregnation and infiltration between nanofibers and resin are appropriate.

2.3. Acoustic emission system

The AMSY-6 Vallen, 8-channel AE system with the sampling rate of 2 MHz was employed to record the AE activity. AE signals were

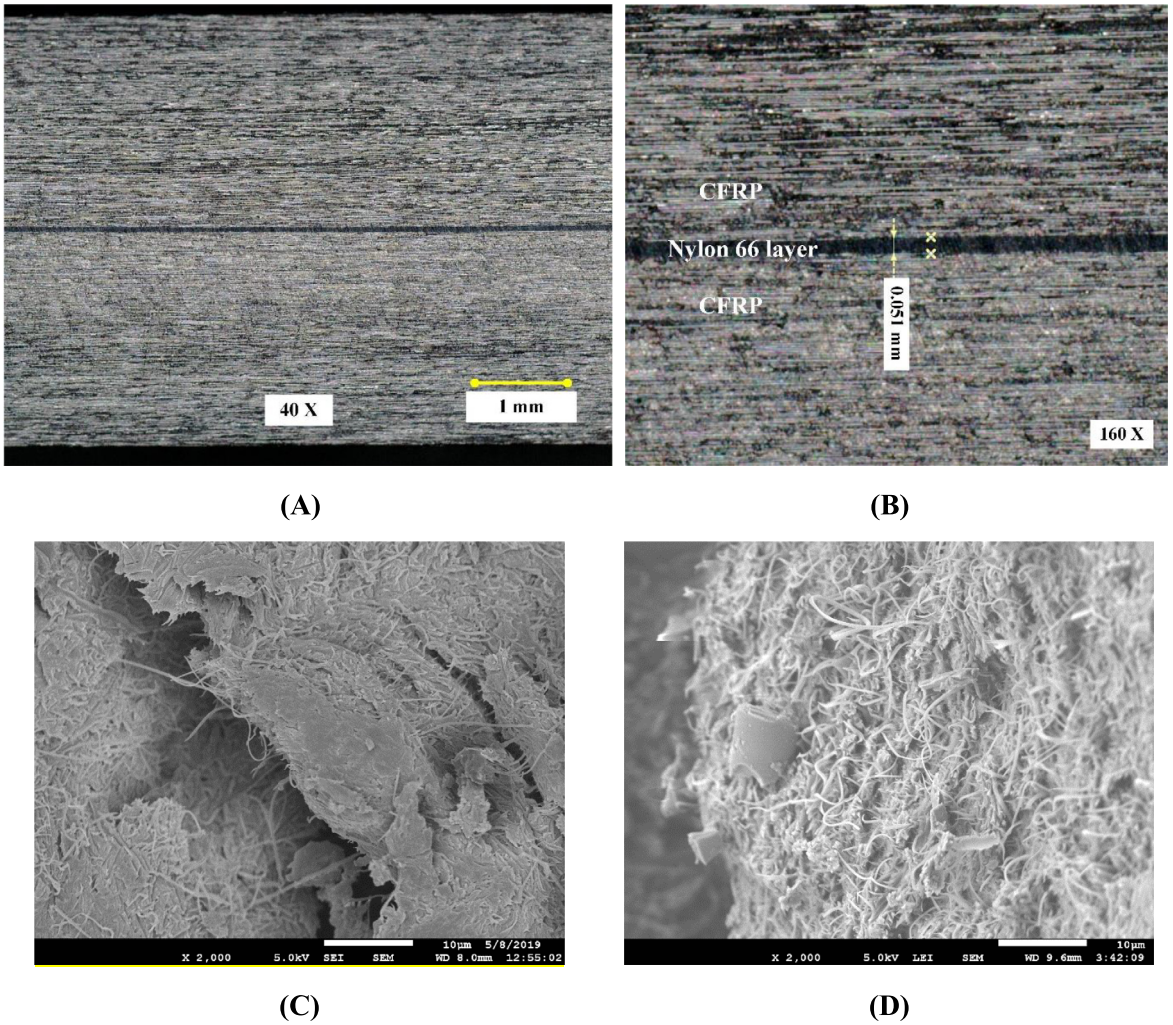

Fig. 3. A & B) The lateral side of the nanomodified specimen at 40× and 160× magnification, respectively, and C & D) the infiltration of the nanofibers and the epoxy resin.

recorded during the loading process using two AE sensors, VS900 M, placed on top of the specimen (see Fig. 4). The sensors were broadband with a frequency range of 100–900 kHz. In order to achieve an appropriate acoustical coupling, the ultrasonic gel was applied at the interface of the sensor and specimen's surface. The AE signals were amplified by 34 dB using a pre-amplifier. The threshold of receiving AE signals was adjusted to 50 dB. A pencil lead break procedure was used to calibrate the data acquisition system and to ensure a good coupling between the AE sensors and the specimen's surface. In order to investigate the effect of attenuation and the damage accumulation on the recorded AE signals, the wave velocity and the attenuation were measured for the specimens at the pristine state and after the fracture toughness test using the pencil lead breakage test [38]. The wave velocity for both virgin and modified specimens was ~8500 m/s for both the pristine state and after the fracture toughness test. In the pristine state, the attenuation was 0.07 and 0.3 dB/cm for the virgin and the modified specimens, while it increased to 0.3 and 0.7 dB/cm for the virgin and the modified specimens after the fracture toughness test. It reveals that the damage accumulation increased the attenuation of the wave in the specimen. However, by considering the small size of the double cantilever beam (DCB) and end-notch flexure (ENF) specimens, the results stated that the attenuation and the damage accumulation did not have a critical effect on the recorded AE signals in the present study. This is consistent with the literature [39]. It is worth mentioning that these phenomena should be considered if the results of this study would be generalized to a real large composite structure.

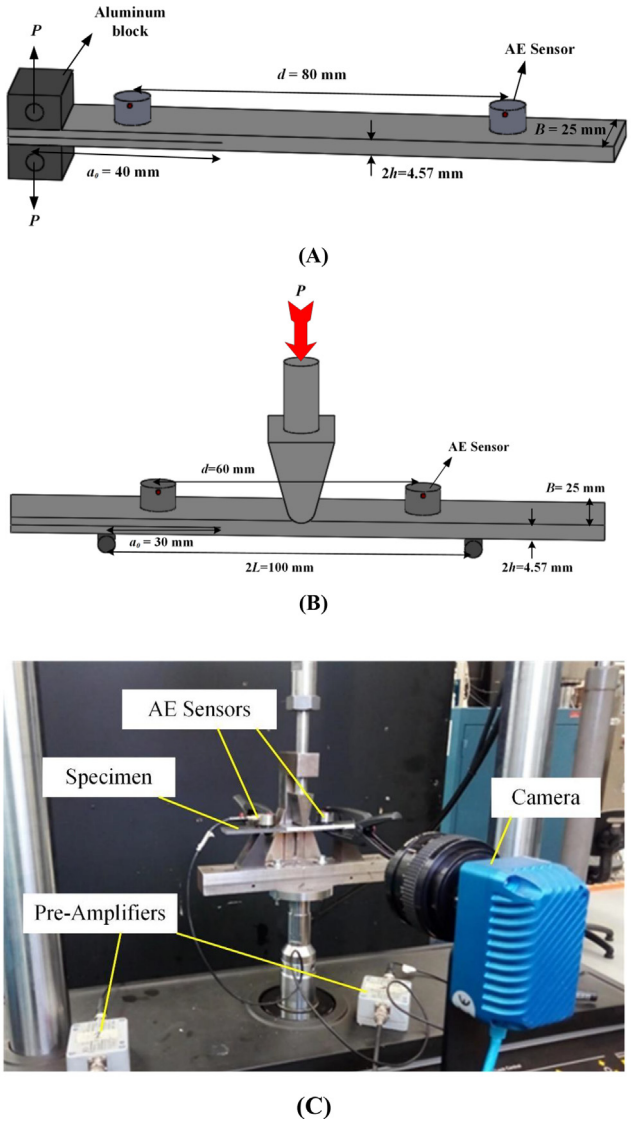

Fig 4. The dimensions of A) DCB and B) ENF specimens, and C) the mode-II test setup.

2.4. Test procedure

The modes I and II fracture tests were conducted according to ASTM D5528 [40] and ASTM D7905M [41], respectively. According to Fig. 4A, the dimensions of the DCB specimen were as follows: the width (B): 25 mm, the initial crack length (a_0): 40 mm, and the thickness (2 h): 4.57 mm. The dimensions of the ENF specimen were as follows: the width (B): 25 mm, the initial crack length (a_0): 30 mm, and the thickness (2 h): 4.57 mm. For the ENF specimens, the distance between two lower roller supports was 100 mm and the AE sensors were located at the two sides of the load point with a distance of 30 mm (Fig. 4B). The specimens were loaded under displacement control mode with a constant displacement rate of 1 mm/min and 0.5 mm/min for mode-I and mode-II, respectively. For applying the load on the DCB specimens, two aluminum blocks were attached to the end of the specimens (Fig. 4A). The load and displacement were continuously recorded during the tests. The crack length was also measured using a digital camera (Fig. 4C) put at the lateral side of the specimen. It is worth mentioning that three specimens were tested for each condition to guarantee the reproducibility of the data.

3. Results and discussion

3.1. The effect of the nanofibers on the fracture toughness

Fig. 5A and B present load–displacement curves of the non-modified (reference) and nanomodified specimens under mode-I and mode-II loading conditions, respectively. As seen, when the specimens were interleaved by nanofibers, the maximum fracture load (P_{cr}) and its corresponding displacement (δ_{cr}) significantly increased, as reported in Table 2. According to Fig. 5A, for mode I loading, the average maximum forces of the reference and modified specimens are 79.52 N and 109.02 N, respectively. Similar results were obtained for mode-II tests, in which P_{cr} values of the reference and nanomodified specimens are 1108.59 N and 1754.7 N, respectively.

In order to calculate the fracture toughness of the specimens at mode-I, ASTM-D5528 standard [42] was employed. Accordingly, the mode-I interlaminar fracture toughness (G_{IC}) is calculated by Eq. (1):

$$G_{IC} = \frac{3p_{cr}\delta_{cr}}{2B(a_0 + \Delta)} \quad (1)$$

where Δ is the crack length modification parameter which can be determined experimentally by plotting the cube root of compliance ($C^{1/3}$) as a function of the delamination length. The compliance, C, is the ratio of the displacement to the applied load, δ/P. Mode-II interlaminar fracture toughness (G_{IIC}) can also be calculated using Eq. (2):

$$G_{IIC} = \frac{3mp_{cr}^2 a_0^2}{2B} \quad (2)$$

where m is the compliance calibration (CC) coefficient explained with detail in ASTM-D7905M standard [41]. Table 2 shows the mode-I and mode-II fracture toughness values and other parameters obtained from the tests. As it can be seen, the average value of G_{IC} is 0.179 ± 0.01 kJ/m^2 and 0.403 ± 0.01 kJ/m^2 for the reference and modified specimens, respectively, which indicates nanofibers increased the mode I fracture toughness by 125%. The average value of G_{IIC} is 0.967 ± 0.005 and 2.533 ± 0.05 for the reference and modified specimens, respectively, that shows a 162% enhancement of the fracture toughness. Because of the good consistency of the results of the three

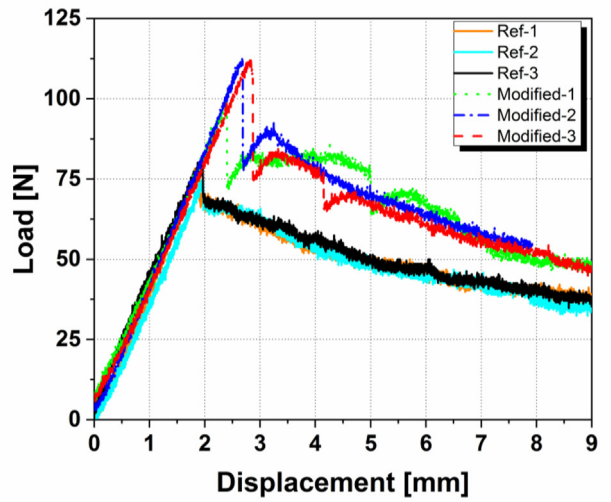

(A)

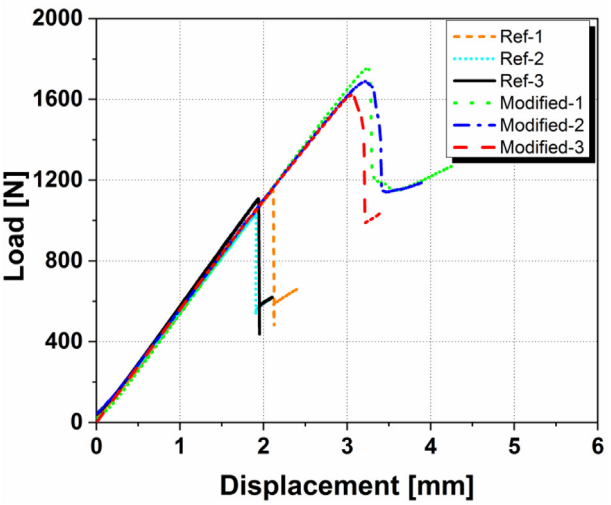

(B)

Fig. 5. Load-displacement curves for the reference and modified specimens; A) mode-I, and B) mode-II tests.

repetitions for each condition, hereafter the results are just presented for one specimen as a representative case.

3.2. The effect of the nanofibers on the damage mechanisms

In the previous section, it was revealed that the nanofibers could significantly increase the fracture toughness (125% and 162% for mode I and mode II respectively). In order to find out the phenomenon that resulted in the increase of the fracture toughness, AE and SEM techniques are used to characterize the different damage mechanisms occurred in the specimens during the delamination growth.

3.2.1. Mode-I loading

The cumulative energy of AE signals of the reference and modified specimens, recorded during mode-I loading conditions, is illustrated in Fig. 6. As shown in the figure, AE activities started earlier in the reference specimen in comparison to the modified one, and also the cumulative curve of the reference specimen increased with a higher gradient than the modified specimen. The final values of cumulative energy for the reference and modified specimens are 2.97e+9 eu and 5.85e+8 eu, respectively which indicates the total cumulative AE energy of the reference specimen is about 12 times larger than the modified one. Because the layup, geometry, loading conditions and test configurations for both reference and modified specimens are the same, this huge difference between the total cumulative AE energy of the specimens may reveal the fact that more damages occurred in the reference specimen compared to the modified one.

As Saeedifar and Zarouchas reported in their recently published review paper [1], among all the AE features, amplitude and peak frequency have been treated as the most preferred features for the damage identification in laminated composites. Because the peak frequency shows less dependency on the attenuation and it is also directly related to the type of the damage, i.e. each damage type usually produces a unique frequency range, it is preferred over the amplitude feature. The peak frequency of the AE signals versus time for the reference and nanomodified laminates is depicted in Fig. 7. As it is visible in the figure, the main AE activities of the reference specimen started at time 120 s, while for the nanomodified specimen, they started at time 180 s which indicates that the nanofibers postponed the damage initiation in the CFRP specimens. In addition, at least three AE clusters can be distinguished, i.e. $<$ 200 kHz, 200–400 kHz, and $>$ 400 kHz which each cluster started at different time. For both reference and modified specimens, the cluster with the lowest frequency started earlier than the other ones. In the case of the reference specimen, the other two clusters occurred almost at the same time, while for the nanomodified specimen, the cluster with the highest frequency started much later than the cluster with the medium frequency. The total number of AE events for the reference and modified specimens is 64,000 and 11,000 respectively, which is consistent with the cumulative energy results (see Fig. 6) and it shows more AE events for the reference specimen compared to the modified one. On the other hand, unlike the reference specimen, the number of AE events at high frequencies is much less for the modified specimen. This phenomenon proved that interleaving the laminates by nanofibers has changed the damage mechanisms distributions of the specimens. In order to find the corresponding damage mechanisms to these AE frequency ranges, the SEM images of the fractured specimens are employed.

The SEM images taken from the fracture surface of the reference and modified specimens are depicted in Fig. 8. As observed, there are many fiber breakages and fiber/matrix debonding at the fracture surface of the reference laminate (Fig. 8A & B), while no debonded or broken fiber is visible in the nanomodified specimen and its dominant damage mode is matrix cracking (Fig. 8C). This is because the nanofibrous mat covered the surface and did not let carbon fibers to be interlocked each other and to bridge between the adjacent composite layers. Therefore, the occurrence of fiber breakage decreased dramatically. Based on the three dominant damage mechanisms observed in the SEM images, i.e. matrix cracking, matrix/fiber debond-

Table 2
The test parameters and the fracture toughnes values for the reference and modified specimens under mode-I and mode-II loading conditions.

Loading mode	Specimen	δ_{cr} (mm)	P_{cr} (N)	(mm)	m (1/N.mm^2)	G_C (kJ/m^2)
Mode- I	Reference	1.89 ± 0.03	79.52 ± 5.1	10.46 ± 2.57	–	0.179 ± 0.01
	Nanomodified	2.81 ± 0.12	109.02 ± 2.8	5.45 ± 1.56	–	0.403 ± 0.01
Mode- II	Reference	2.08 ± 0.11	1097.6 ± 61.6	–	1.49E−08 ± 1.04E−09	0.967 ± 0.005
	Nanomodified	3.22 ± 0.14	1689.52 ± 65.3	–	1.65E−08 ± 3.06E−10	2.533 ± 0.05

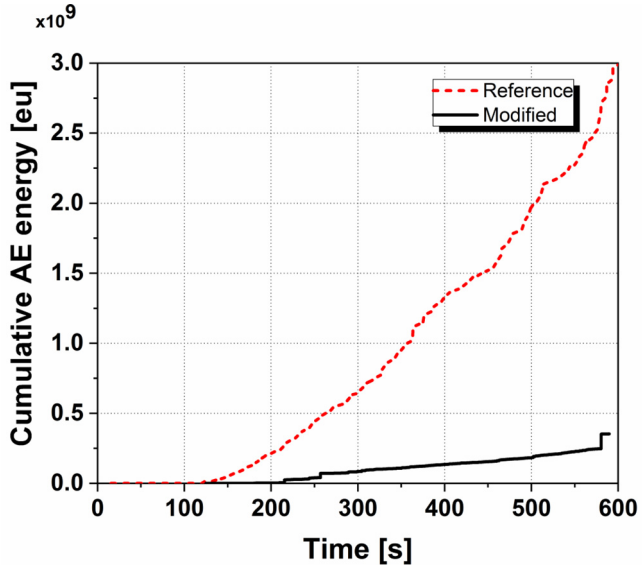

Fig 6. The behavior of cumulative AE energy during mode-I loading test.

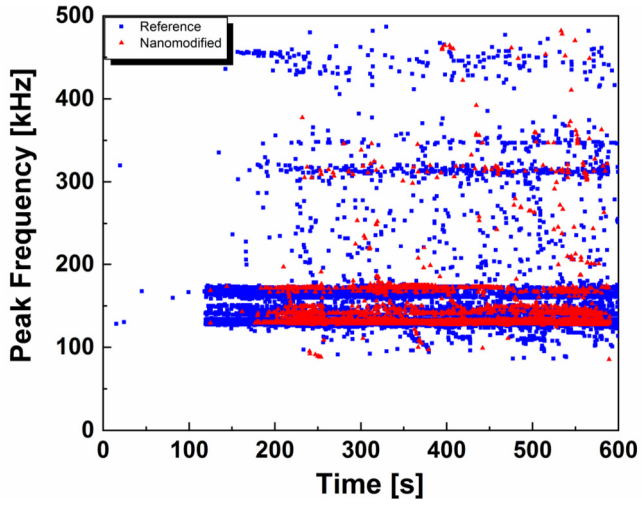

Fig. 7. The peak frequency vs time for the mode I test.

ing and fiber breakage, the AE signals clusters will be allocated to these damage mechanisms.

Among the unsupervised techniques used in the literature for the AE data clustering, the hierarchical method has shown high levels of confidence and repeatability of the clustering results [1]. Therefore, in the present study, this model is used for the clustering of the AE data. The clustering process is done in the following four steps:

1. If the total number of data points is n, each data point is first considered as a separate cluster. Therefore, each cluster has just one member which is the representative of the cluster's centroid as well.
2. In this step, the dissimilarity of the clusters is calculated. The Centroid linkage (d) was considered as the dissimilarity metric which calculates the Euclidean distance between the centroids of the two clusters. It is worth mentioning that after the first iteration, the centroid of each cluster is considered as the average of its members (Eq. (4)).

$$d(r,s) = \|\overline{x_r} - \overline{x_s}\|_2 \tag{3}$$

$$\overline{x_r} = \frac{1}{n_r}\sum_{i=1}^{n_r} x_{ri} \tag{4}$$

where $d(r,s)$ is the metric, $\overline{x_r}$ indicates the centroid of the cluster r, and n_r and x_{ri} show the number of data points and the value of the data points within the cluster r.

3. Then, the two clusters with the lowest Centroid linkage value are merged together. Therefore, the number of clusters is reduced by one unit.
4. Steps 2 and 3 are repeated until the stop criterion is achieved, which is usually the desired number of the clusters.

Based on the three dominant damage mechanisms observed in the SEM images, i.e. matrix cracking, matrix/fiber debonding and fiber breakage, the AE signals were distinguished into 3 clusters using the hierarchical method. Fig. 9 shows the clustered AE data by the hierarchical method for the reference and nanomodified specimens. The frequency ranges for the 1st, 2nd and 3rd clusters are $<$ 200 kHz, [200–400 kHz] and $>$ 400 kHz, respectively. These frequency ranges are similar to the frequency ranges reported in the literature for the CFRP composites (see Table 3). According to the table, the matrix cracking has the lowest frequency content, the fiber breakage has the highest frequency, and the frequency of the fiber/matrix debonding is between the frequency values of these two damages. Therefore, the cluster 1 with the lowest frequency content, $<$200 kHz, was dedicated to the matrix cracking, the cluster 3 with the highest frequency content, $>$400 kHz, was devoted to the fiber breakage, and the cluster 2 with a frequency content between the frequency of these two clusters was allocated to the fiber/matrix debonding. In the case of the modified specimen, the AE results show that the number of signals within clusters 2 and 3 (fiber /matrix debonding and fiber breakage) are considerably reduced compared to the reference specimen. This result is consistent with the SEM observations (see Fig. 8), which indicated that the number of fiber breakages and fiber/matrix debonding significantly reduced in the modified specimen compared to the reference one.

The cumulative energy of the AE signals for each cluster was calculated and it is plotted in Fig. 10. As it is seen, matrix cracking signals initiated before fiber breakage and fiber/matrix debonding signals for both reference and nanomodified specimens. Table 4 summarizes the total values of the cumulative AE energy for each damage type. As seen, all damage mechanisms, i.e. matrix cracking, fiber/matrix debonding and fiber breakage, decreased by 91.9%, 26.7% and 87.4%, respectively, by applying nanofibrous mat between composite's layers.

3.2.2. Mode-II loading

It is worth mentioning that for both reference and modified specimens, the mode II test was stopped while the crack tip reached the loading roller. This is due to the fact that high compression stresses existed in the area under the loading roller arrested the crack to propagate further by increasing the load. According to Fig. 11, the total cumulative AE energy values of the reference and modified specimens were 41.12e+7 eu and 1.3e+7 eu, respectively. It may reveal that more damages occurred in the reference specimen compared to the modified one while crack grew to reach the loading roller. In addition, cumulative energy curves show that the nanofibers postponed the start of the AE activities, from time of 100 s for the reference specimen to 250 s for the modified specimen.

Fig. 12 illustrates the SEM image taken from the fracture surface of the mode II reference and modified specimens. As observed, the dominant damage mechanisms are matrix cracking and fiber imprint, which indicates fiber/matrix debonding, and no broken fiber is visible on the fracture surface.

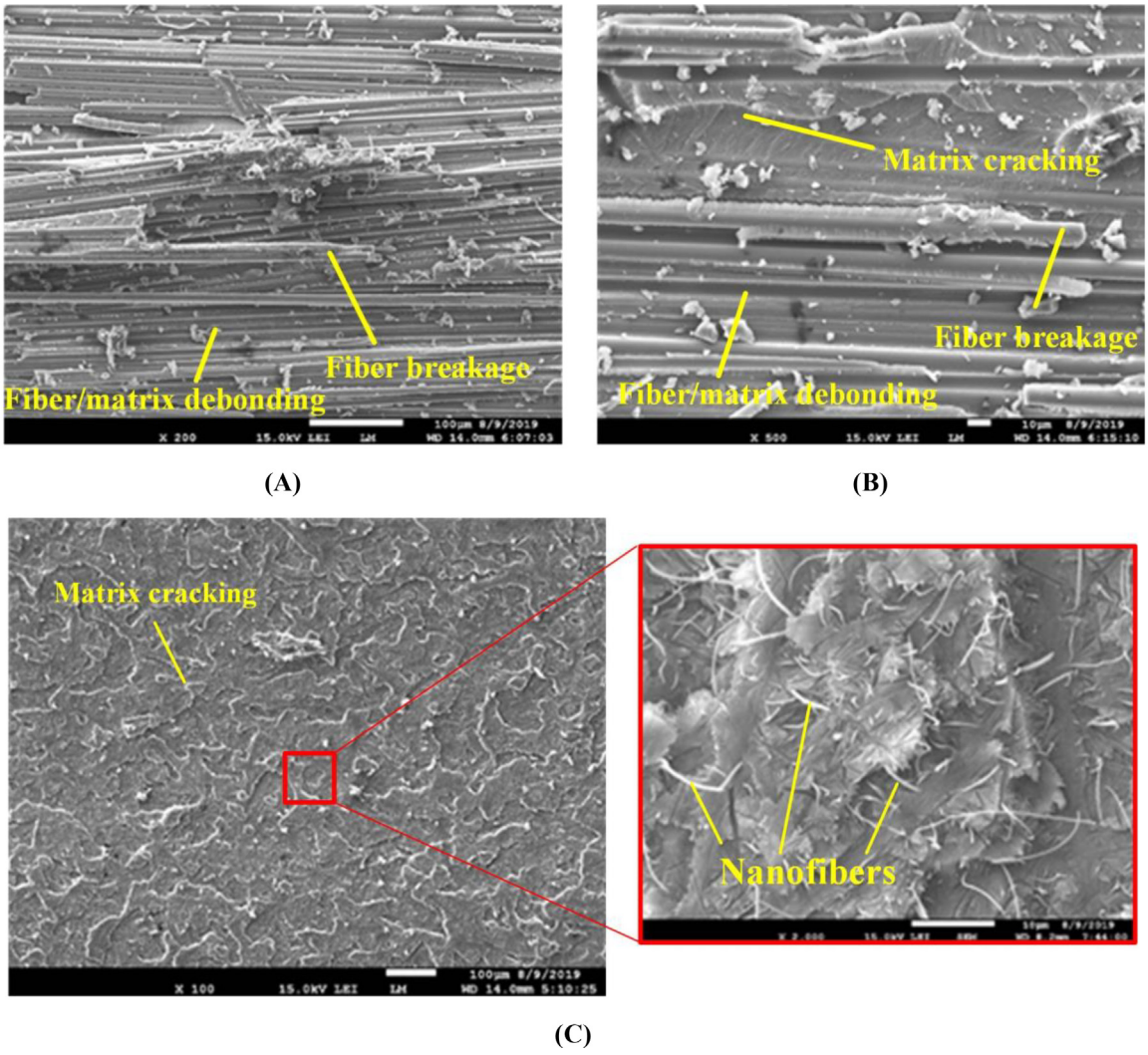

Fig. 8. The SEM micrographs of the fractured surface under mode-I loading; A & B) the reference specimen at 200× and 500× magnification, respectively, and C) the nanomodified specimen.

Fig. 13 shows the distribution of the AE peak frequency for the specimens. As seen, there are a huge number of signals with the frequency of <200 kHz for both reference and modified specimens, while there are just a few signals with the frequency range of [200–400 kHz] and there is no signal with the frequency range of >400 kHz. Therefore, according to the frequency ranges allocated to the damage mechanisms for the mode I loading conditions, AE shows that no fiber breakage occurred in both specimens which is consistent with the SEM images (see Fig. 12). In addition, the signals related to the fiber/matrix debonding, [200–400 kHz], occurred at the end of the test, around the maximum load, while the matrix cracking signals, <200 kHz, appeared much earlier at the early stages of the loading.

To describe the consequence of the occurring of the damage mechanisms, a schematic is shown in Fig. 14. The stress state ahead of the crack tip and the matrix cracking initiation under interlaminar mode-II shear loading are illustrated in Fig. 14A. As seen, the tensile traction (σ_R) is inclined at an angle of 45° to the laminate plane which causes the angled cracks to form. Consequently, angled cracks are developed in the matrix ahead of the crack tip. As the load increases, these angled cracks start to be extended along the 45° lines (Fig. 14B) [49]. According to Fig. 14B, the angled matrix cracks are created at the beginning of the test (Points 1 and 2) and they are enhanced by increasing the load level (Point 3). The initial AE signals of the matrix cracks were captured here (see Fig. 13). When these cracks are saturated at the process zone (Point 4), the adjacent layers are suddenly separated from each other and the fiber/matrix debonding occurs. This is the point that the signals related to the fiber/matrix debonding, [200–400 kHz], were captured by the AE sensors (see Fig. 13).

Table 5 presents the values of the cumulative AE energy for each damage mechanism. As seen, the corresponding cumulative energy to the fiber breakage is zero for both reference and modified specimens. Furthermore, cumulative AE energy values related to the matrix cracking and fiber/matrix debonding mechanisms are decreased by 96.8% and 97.3%, respectively, by applying the nanofibers.

3.2.3. Sentry function analysis

The sentry function, defined as the logarithm of the ratio of mechanical energy over the AE energy, has been widely used for the damage evolution analysis in laminated composites (Eq. (5)). According to the literature [46], based on the damage state of the specimen, the sentry function indicates four different trends:

1) The increasing trend: It indicates the occurring of micro damages in the specimen.

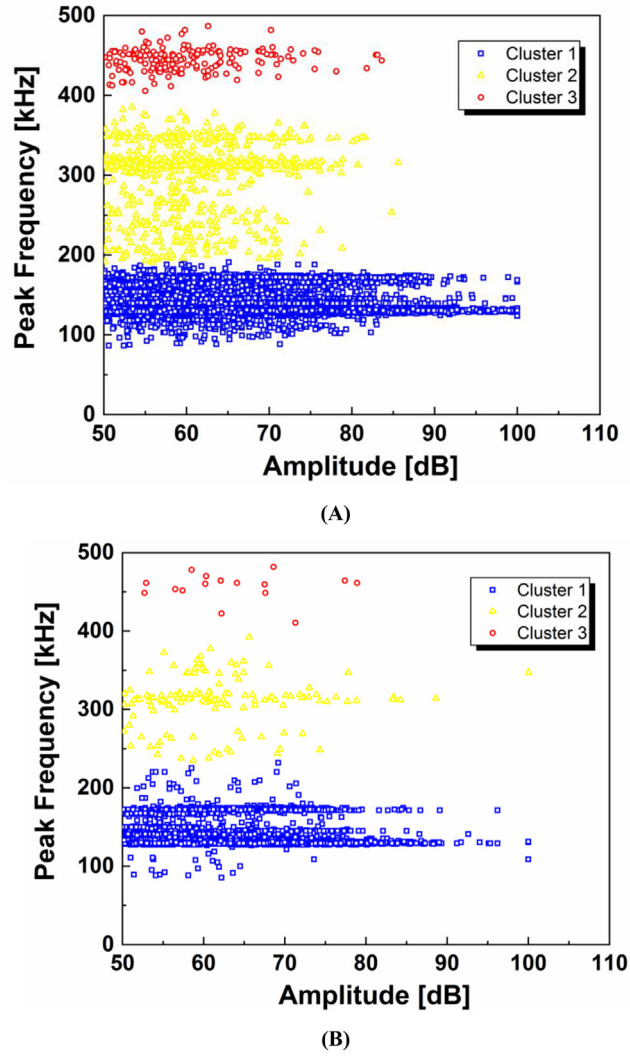

Fig. 9. Clustering of the AE signals using hierarchical model for; A) the reference, and B) the nanomodified specimens.

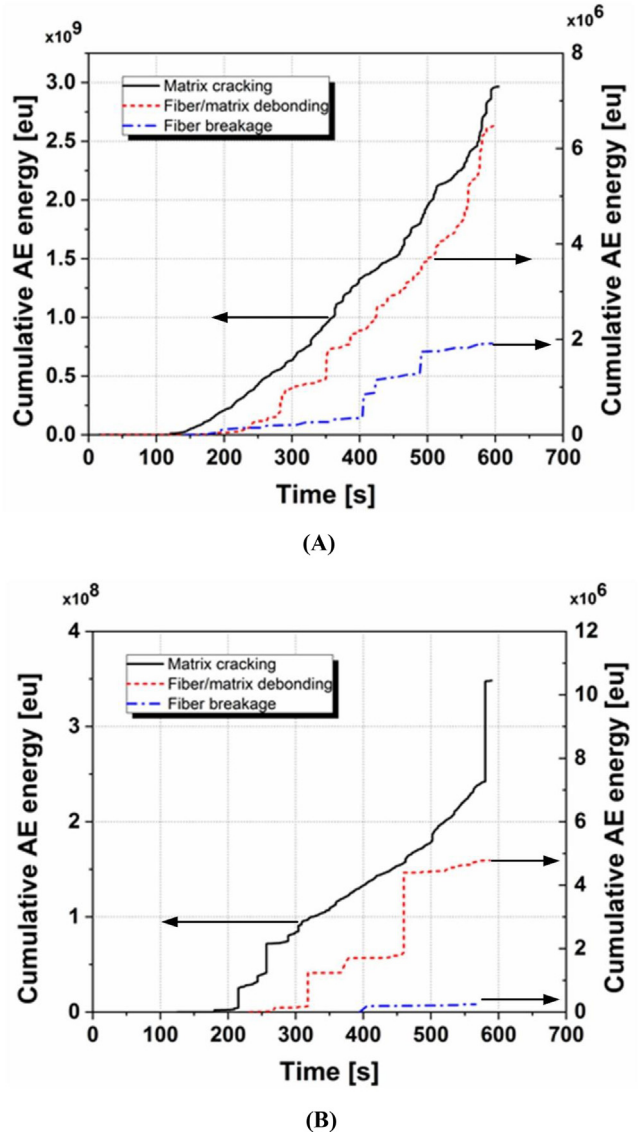

Fig 10. Cumulative of AE energy in mode-I loading test; A) reference, and B) nanomodified.

2) The big drop: It illustrates considerable damage in the specimen.
3) The constant trend: It shows that there is an equilibrium state between the weakening mechanisms, such as damage, and the strengthening mechanisms, such as the fiber bridging or nanofiber toughening.
4) The continuous decreasing trend: It indicates the fact that the damage is propagating within the material and the material cannot resist against it anymore.

$$S(x) = \ln\left[\frac{E_{ME}(x)}{E_{AE}(x)}\right] \quad (5)$$

where $S(x)$ is the sentry function, and E_{ME} (x) and E_{AE} (x) are the mechanical energy and the AE events energy, respectively. The mechanical energy is considered as the area beneath the load–displacement curve and the AE energy is the energy of the AE signals.

Fig. 15 illustrates the sentry function curve for the reference and the nanomodified specimens under mode I and mode II loading conditions. In the case of mode I loading conditions, the sentry function of the reference specimen started earlier than the nanomodified one, which indicates the micro damages occurred in the reference specimen earlier. For both specimens, the biggest drop happened at the maxi-

Table 3
The frequency range of different damage mechanisms in CFRP composites.

Reference	Material	Test	Matrix cracking	Fiber/matrix debonding	Fiber breakage
[43]	Carbon/epoxy	Tensile	90–180	240–310	>300
[44]	Carbon/epoxy	Tensile, compact tension, compact compression, DCB and ENF	<50	200–300	400–500
[45]	Carbon/epoxy	Tensile	<300	–	>500
[46]	Carbon/epoxy	Indentation	<150	150–300	>400
[47]	Carbon/epoxy	Tensile	–	250–330	>450
[48]	Carbon/epoxy	Tensile	<100	200–300	400–450

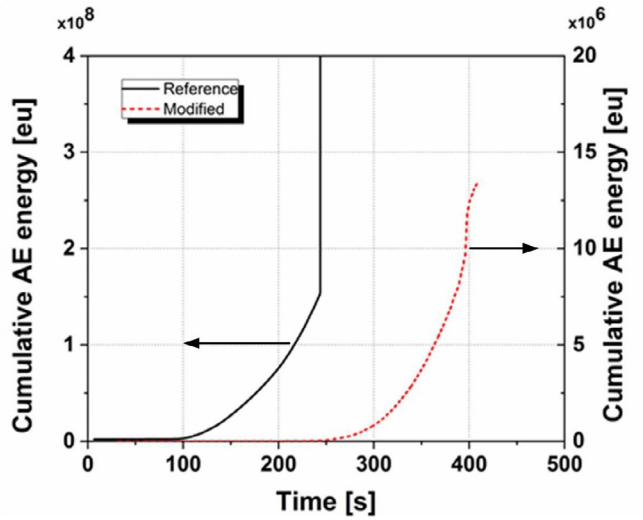

Fig. 11. The cumulative AE energy curves of the reference and modified specimens for the mode II test.

mum load. It is then followed by a continuous decreasing trend for the reference specimen, while in the case of the nanomodified specimen there is a constant trend after the big drop. This indicates that after the maximum load, the reference specimen could not withstand the applied load anymore, while there was an equilibrium state between the damage and nanofibers toughening in the modified specimen. In the case of mode II loading conditions, the trends of the sentry function curves are similar, by the difference that the continuous decreasing trend of the nanomodified specimen started at the load of 907 N, while it started at the load of 415 N for the reference specimen. This indicates that the reference specimen started to be degraded much earlier than the nanomodified specimen.

4. Conclusion

In this study, acoustic emission (AE) and scanning electron microscope (SEM) techniques were used for the quantitative analysis of the different damage mechanisms occurred in carbon/epoxy laminates interleaved by PA66 electrospun nanofibers subjected to the mode-I and mode-II fracture tests. The concluding remarks are summarized as follows:

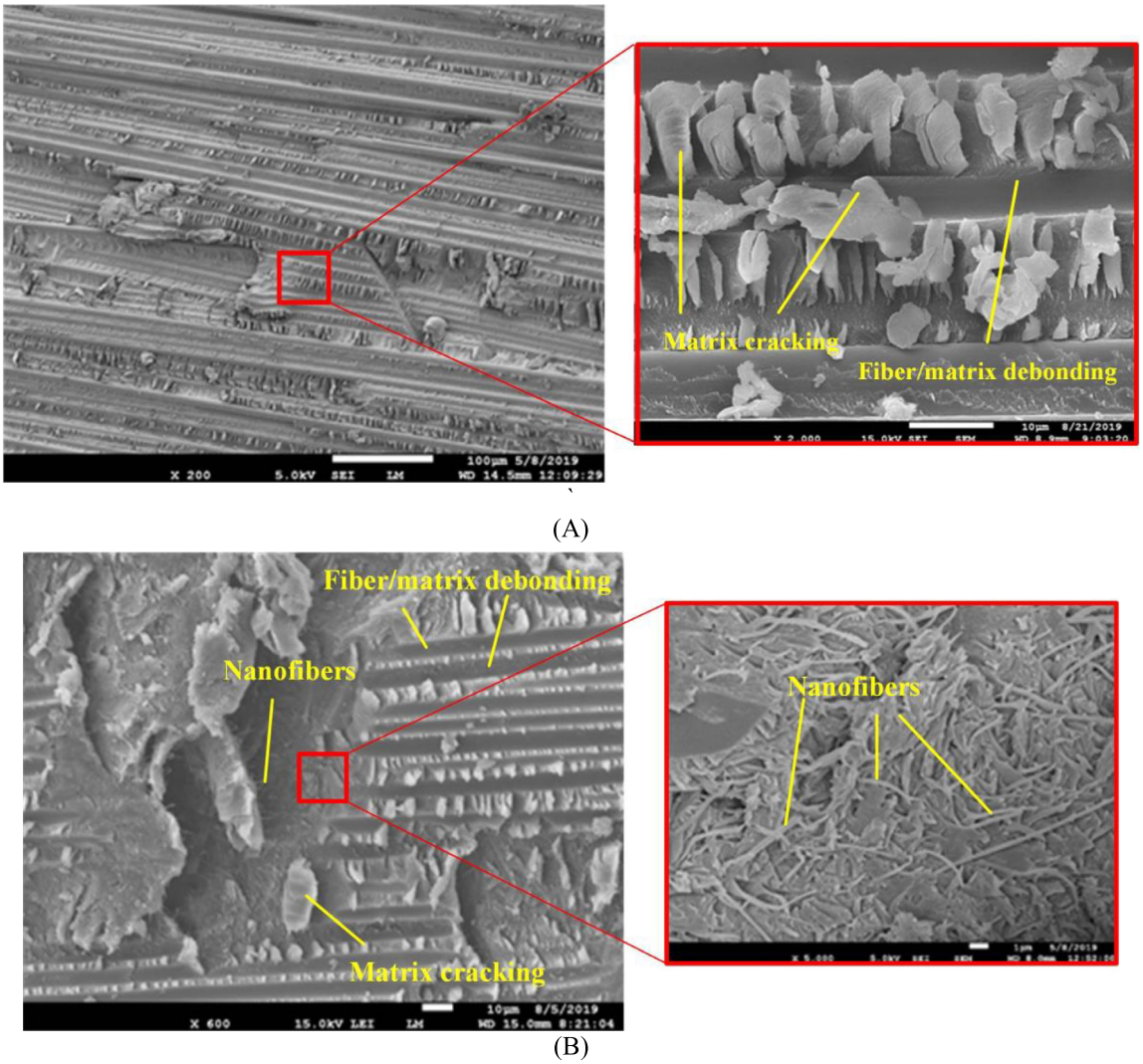

Fig. 12. The mode-II fractured surface of A) reference, and B) nanofiber-modified specimens.

Table 4
The values of cumulative AE energy for different damage mechanisms in the reference and modified specimens under mode-I loading.

Specimen type	Cumulative AE energy (eu)			Total cumulative AE energy (eu)
	Matrix cracking	Fiber/matrix debonding	Fiber breakage	
Reference	29.6E+8	6.52E+6	1.91E+6	29.7E+8
Modified	2.41E+8	4.78E+6	0.24E+6	2.46E+8
Reduction percentage	−91.9%	−26.7%	−87.4%	−91.7%

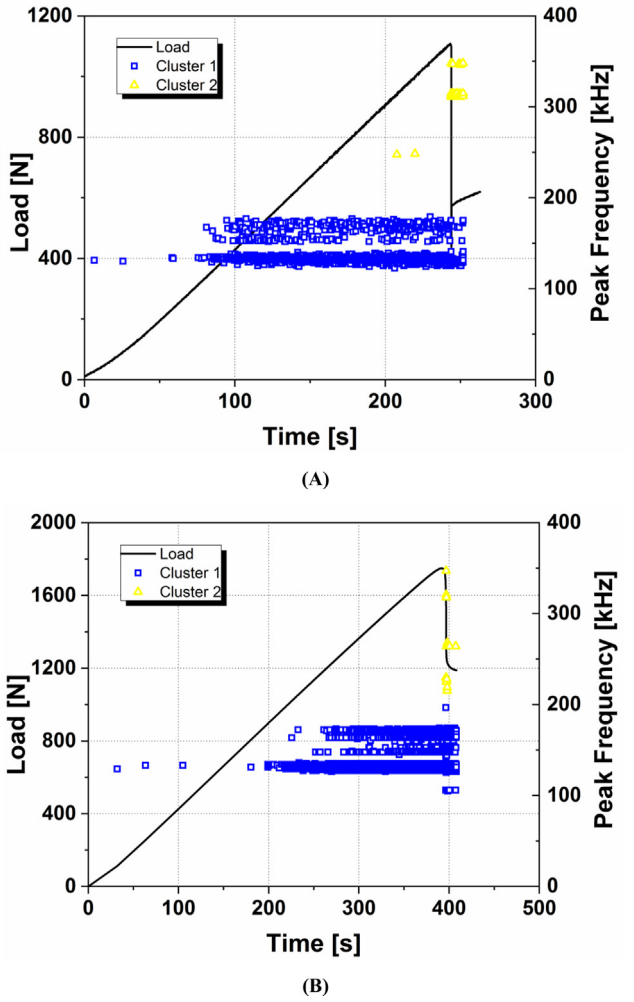

Fig. 13. The AE behavior at mode II loading test; A) reference, and B) nanomodified.

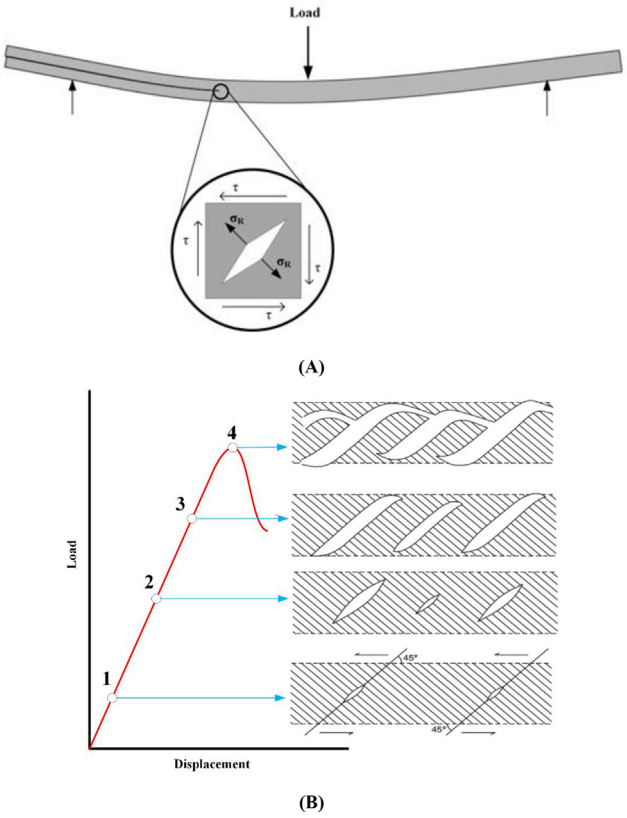

Fig. 14. Damages growth in mode-II loading; A) the stress state and the mechanism of matrix cracking formation, and B) the propagation and coalescence of angled matrix cracks.

1- The modes I and II interlaminar fracture toughness values of the nanomodified specimens were enhanced by 125% and 162% respectively.
2- For the same crack growth length, the number of AE events and the cumulative energy of these events for the nanomodified specimens were much less than the reference specimens which indicated fewer damages occurred in the modified specimens.
3- For the mode I test campaign, the SEM images showed that the nanofibers significantly reduced the fiber breakage and fiber/-matrix debonding by tailoring the fibers to their surrounding matrix.
4- For the mode II test campaign, the SEM images revealed that no fiber breakage occurred in both reference and modified specimens.
5- According to the damage mechanisms observed in the SEM images, i.e. matrix cracking, fiber/matrix debonding and fiber breakage, the AE signals were clustered into three clusters using the hierarchical method. Matrix cracking with the frequency of < 200 kHz, fiber/matrix debonding, [200–400 kHz], and fiber breakage, >400 kHz.
6- The AE results were consistent with the SEM observation which showed a considerable decrease of fiber breakage and fiber/matrix debonding for the modified specimens under mode I test. They also showed that no fiber breakage signal existed for both reference and modified specimens under mode II test, as already had been observed in the SEM images.
7- AE results revealed that the PA66 nanofibers led to the decrease of the matrix cracking, fiber/matrix debonding and fiber breakage by 92%, 27%, and 87%, respectively under mode I loading conditions. For the mode II test, both matrix cracking and fiber/matrix debonding decreased by 97%, and no fiber breakage signal was observed for both reference and modified specimens.

Table 5
The values of cumulative AE energy for different damage mechanisms for the reference and modified specimens under mode-II loading.

Specimen type	Cumulative AE energy (eu)			Total cumulative AE energy (eu)
	Matrix cracking	Fiber/matrix debonding	Fiber breakage	
Reference	4.11E+8	0.19E+6	0	4.112E+8
Modified	0.13E+8	0.005E+6	0	0.13E+8
Reduction percentage	−96.8%	−97.3%	–	−96.8%

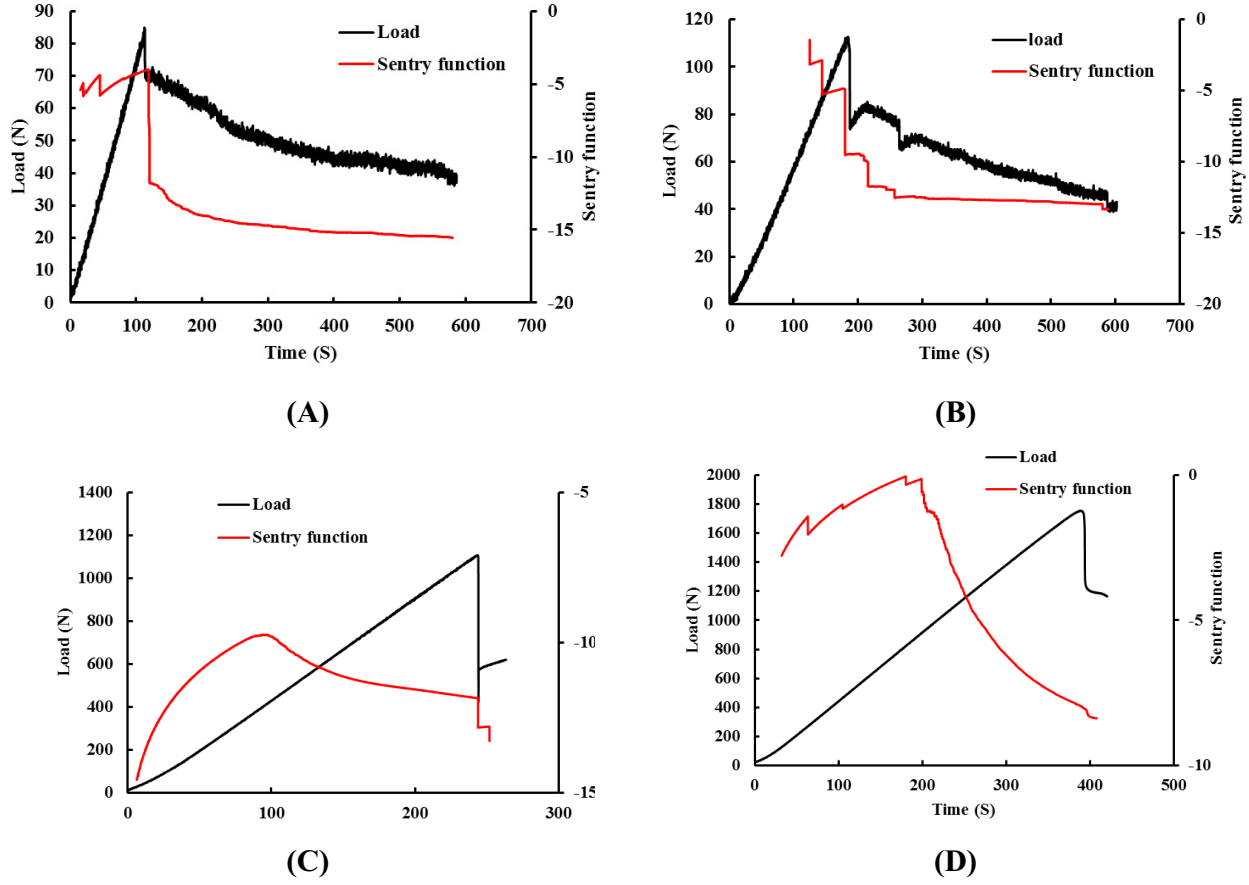

Fig. 15. The sentry function curve of A) the reference specimen under mode I loading, B) the modified specimen under mode I loading, C) the reference specimen under mode II loading, and D) the modified specimen under mode II loading.

CRediT authorship contribution statement

Reza Mohammadi: Validation, Formal analysis, Investigation, Data curation, Writing - original draft, Visualization, Writing - review & editing. **Mehdi Ahmadi Najafabadi:** Conceptualization, Supervision, Resources, Project administration, Funding acquisition, Writing - review & editing. **Hamed Saghafi:** Conceptualization, Investigation, Resources, Writing - original draft, Project administration, Writing - review & editing. **Milad Saeedifar:** Investigation, Formal analysis, Writing - original draft, Writing - review & editing. **Dimitrios Zarouchas:** Supervision, Resources, Project administration, Funding acquisition, Writing - review & editing.

Declaration of Competing Interest

The authors declare that they have no known competing financial interests or personal relationships that could have appeared to influence the work reported in this paper.

References

[1] Saeedifar M, Zarouchas D. Damage characterization of laminated composites using acoustic emission: a review. Compos B Eng 2020;195.
[2] Minak G, Zucchelli A. Damage evaluation and residual strength prediction of CFRP laminates by means of acoustic emission techniques. Durand, LP (ed) Composite Materials Research Progress. 2008:165-207.
[3] Yousefi J, Ahmadi M, Shahri MN, Oskouei AR, Moghadas FJ. Damage categorization of glass/epoxy composite material under mode ii delamination using acoustic emission data: a clustering approach to elucidate wavelet transformation analysis. Arab J Sci Eng 2014;39:1325–35.
[4] Jiang W, Yao W, Qi W, Shen H. Study on the fractal dimension and evolution of matrix crack in cross-ply GFRP laminates. Theor Appl Fract Mech 2020;102478.
[5] Saeedifar M, Ahmadi Najafabadi M, Mohammadi K, Fotouhi M, Hosseini Toudeshky H, Mohammadi R. Acoustic emission-based methodology to evaluate delamination crack growth under quasi-static and fatigue loading conditions. J Nondestr Eval 2017;37:1.
[6] Saeedifar M, Mansvelder J, Mohammadi R, Zarouchas D. Using passive and active acoustic methods for impact damage assessment of composite structures. Compos Struct 2019;226.
[7] Gu B, Zhang H, Wang B, Zhang S, Feng X. Fracture toughness of laminates reinforced by piezoelectric z-pins. Theor Appl Fract Mech 2015;77:35–40.

[8] Moghimi Monfared R, Ayatollahi MR, Barbaz Isfahani R. Synergistic effects of hybrid MWCNT/nanosilica on the tensile and tribological properties of woven carbon fabric epoxy composites. Theor Appl Fract Mech 2018;96:272–84.
[9] Zhang D, Zheng X, Wang Z, Wu T, Sohail A. Effects of braiding architectures on damage resistance and damage tolerance behaviors of 3D braided composites. Compos Struct 2020;232.
[10] Gholizadeh A, Najafabadi MA, Saghafi H, Mohammadi R. Considering damage during fracture tests on nanomodified laminates using the acoustic emission method. Eur J Mech A Solids 2018;72:452–63.
[11] Neisiany RE, Khorasani SN, Lee JKY, Naeimirad M, Ramakrishna S. Interfacial toughening of carbon/epoxy composite by incorporating styrene acrylonitrile nanofibers. Theor Appl Fract Mech 2018;95:242–7.
[12] Razavi SMJ, Neisiany RE, Ayatollahi MR, Ramakrishna S, Khorasani SN, Berto F. Fracture assessment of polyacrylonitrile nanofiber-reinforced epoxy adhesive. Theor Appl Fract Mech 2018;97:448–53.
[13] Saghafi H, Moallemzadeh AR, Zucchelli A, Brugo TM, Minak G. Shear mode of fracture in composite laminates toughened by polyvinylidene fluoride nanofibers. Compos Struct 2019;227.
[14] Mohammadi R, Najafabadi MA, Saghafi H, Zarouchas D. Mode-II fatigue response of AS4/8552 carbon /epoxy composite laminates interleaved by electrospun nanofibers. Thin-Walled Struct 2020;154.
[15] Yudhanto A, Watanabe N, Iwahori Y, Hoshi H. Compression properties and damage mechanisms of stitched carbon/epoxy composites. Compos Sci Technol 2013;86:52–60.
[16] Zheng N, Huang Y, Liu H-Y, Gao J, Mai Y-W. Improvement of interlaminar fracture toughness in carbon fiber/epoxy composites with carbon nanotubes/polysulfone interleaves. Compos Sci Technol 2017;140:8–15.
[17] Li P, Liu D, Zhu B, Li B, Jia X, Wang L, et al. Synchronous effects of multiscale reinforced and toughened CFRP composites by MWNTs-EP/PSF hybrid nanofibers with preferred orientation. Compos A Appl Sci Manuf 2015;68:72–80.
[18] Li G, Li P, Zhang C, Yu Y, Liu H, Zhang S, et al. Inhomogeneous toughening of carbon fiber/epoxy composite using electrospun polysulfone nanofibrous membranes by in situ phase separation. Compos Sci Technol 2008;68:987–94.
[19] Saghafi H, Minak G, Zucchelli A, Brugo TM, Heidary H. Comparing various toughening mechanisms occurred in nanomodified laminates under impact loading. Compos B Eng 2019;174.
[20] Saghafi H, Brugo T, Minak G, Zucchelli A. Improvement the impact damage resistance of composite materials by interleaving Polycaprolactone nanofibers. Eng Solid Mech 2015;3:21–6.
[21] Zheng N, Liu H-Y, Gao J, Mai Y-W. Synergetic improvement of interlaminar fracture energy in carbon fiber/epoxy composites with nylon nanofiber/polycaprolactone blend interleaves. Compos B Eng 2019;171:320–8.
[22] van der Heijden S, Daelemans L, Meireman T, De Baere I, Rahier H, Van Paepegem W, et al. Interlaminar toughening of resin transfer molded laminates by electrospun polycaprolactone structures: effect of the interleave morphology. Compos Sci Technol 2016;136:10–7.
[23] Saghafi H, Ghaffarian S, Brugo T, Minak G, Zucchelli A, Saghafi H. The effect of nanofibrous membrane thickness on fracture behaviour of modified composite laminates–A numerical and experimental study. Compos B Eng 2016;101:116–23.
[24] Zhang J, Yang T, Lin T, Wang CH. Phase morphology of nanofibre interlayers: Critical factor for toughening carbon/epoxy composites. Compos Sci Technol 2012;72:256–62.
[25] Magniez K, De Lavigne C, Fox BL. The effects of molecular weight and polymorphism on the fracture and thermo-mechanical properties of a carbon-fibre composite modified by electrospun poly (vinylidene fluoride) membranes. Polymer 2010;51:2585–96.
[26] Ipackchi H, Rezadoust AM, Esfandeh M, Rezaei M. Improvement of interlaminar fracture toughness of phenolic laminates interleaved with electrospun polyvinyl butyral nanofibers. Theor Appl Fract Mech 2020;105.
[27] Barzoki PK, Rezadoust AM, Latifi M, Saghafi H, Minak G. Effect of nanofiber diameter and arrangement on fracture toughness of out of autoclave glass/phenolic composites – Experimental and numerical study. Thin-Walled Struct 2019;143.
[28] Barzoki PK, Rezadoust A, Latifi M, Saghafi H. The experimental and numerical study on the effect of PVB nanofiber mat thickness on interlaminar fracture toughness of glass/phenolic composites. Eng Fract Mech 2018;194:145–53.
[29] Saghafi H, Fotouhi M, Minak G. Improvement of the impact properties of composite laminates by means of nano-modification of the Matrix—A review. Appl Sci 2018;8:2406.
[30] Gholizadeh A, Najafabadi MA, Saghafi H, Mohammadi R. Considering damages to open-holed composite laminates modified by nanofibers under the three-point bending test. Polym Test 2018;70:363–77.
[31] Palazzetti R, Zucchelli A, Trendafilova I. The self-reinforcing effect of Nylon 6,6 nano-fibres on CFRP laminates subjected to low velocity impact. Compos Struct 2013;106:661–71.
[32] Mohammadi R, Najafabadi MA, Saghafi H, Zarouchas D. Fracture and fatigue behavior of carbon/epoxy laminates modified by nanofibers. Compos A Appl Sci Manuf 2020;137.
[33] Akangah P, Lingaiah S, Shivakumar K. Effect of Nylon-66 nano-fiber interleaving on impact damage resistance of epoxy/carbon fiber composite laminates. Compos Struct 2010;92:1432–9.
[34] Brugo T, Palazzetti R. The effect of thickness of Nylon 6,6 nanofibrous mat on Modes I-II fracture mechanics of UD and woven composite laminates. Compos Struct 2016;154:172–8.
[35] Palazzetti R, Yan X, Zucchelli A. Influence of geometrical features of electrospun nylon 6,6 interleave on the CFRP laminates mechanical properties. Polym Compos 2014;35:137–50.
[36] Palazzetti R, Zucchelli A, Gualandi C, Focarete ML, Donati L, Minak G, et al. Influence of electrospun Nylon 6,6 nanofibrous mats on the interlaminar properties of Gr–epoxy composite laminates. Compos Struct 2012;94:571–9.
[37] HexPly® 8552 Epoxy matrix (180°C/356°F curing matrix) in FTA 072e. In: Publication HC, editor.2013.
[38] International A. ASTM E976–10, Standard guide for determining the reproducibility of acoustic emission sensor response. West Conshohocken, PA.: ASTM International; 2010.
[39] Zhou W, Zhao W-Z, Zhang Y-N, Ding Z-J. Cluster analysis of acoustic emission signals and deformation measurement for delaminated glass fiber epoxy composites. Compos Struct 2018;195:349–58.
[40] ASTM D5528-13, Standard Test Method for Mode I Interlaminar Fracture Toughness of Unidirectional Fiber-Reinforced Polymer Matrix Composites, ASTM International, West Conshohocken, PA, 2013, www.astm.org.
[41] ASTM D7905/D7905M–14. Standard Test Method for Determination of the Mode II Interlaminar Fracture Toughness of Unidirectional Fiber-Reinforced Polymer Matrix Composites. 2014.
[42] Zhang C, Li N, Wang W, Binienda W, Fang H. Progressive damage simulation of triaxially braided composite using a 3D meso-scale finite element model. Compos Struct 2015;104–16.
[43] de Groot PJ, Wijnen PAM, Janssen RBF. Real-time frequency determination of acoustic emission for different fracture mechanisms in carbon/epoxy composites. Compos Sci Technol 1995;55:405–12.
[44] Gutkin R, Green CJ, Vangrattanachai S, Pinho ST, Robinson P, Curtis PT. On acoustic emission for failure investigation in CFRP: Pattern recognition and peak frequency analyses. Mech Syst Sig Process 2011;25:1393–407.
[45] Komai K, Minoshima K, Shibutani T. Investigations of the Fracture Mechanism of Carbon/Epoxy Composites by AE Signal Analyses. JSME international journal Ser 1, Solid mechanics, strength of materials. 1991;34:381-8.
[46] Saeedifar M, Najafabadi MA, Zarouchas D, Toudeshky HH, Jalalvand M. Clustering of interlaminar and intralaminar damages in laminated composites under indentation loading using Acoustic Emission. Compos B Eng 2018;144:206–19.
[47] Chou HY, Mouritz AP, Bannister MK, Bunsell AR. Acoustic emission analysis of composite pressure vessels under constant and cyclic pressure. Compos A Appl Sci Manuf 2015;70:111–20.
[48] Ni Q-Q, Iwamoto M. Wavelet transform of acoustic emission signals in failure of model composites. Eng Fract Mech 2002;69:717–28.
[49] Greenhalgh E. Failure analysis and fractography of polymer composites. Failure Anal Fractogr Polym Compos 2009:1–595.